

Global simulations of strongly magnetized remnant massive neutron stars formed in binary neutron star mergers

Kenta Kiuchi,¹ Koutarou Kyutoku,^{2,3,4,1} Yuichiro Sekiguchi,^{5,1} and Masaru Shibata¹

¹*Center for Gravitational Physics, Yukawa Institute for Theoretical Physics, Kyoto University, Kyoto, 606-8502, Japan*

²*Theory Center, Institute of Particle and Nuclear Studies, KEK, Tsukuba 305-0801, Japan*

³*Department of Particle and Nuclear Physics, the Graduate*

University for Advanced Studies (Sokendai), Tsukuba 305-0801, Japan

⁴*Interdisciplinary Theoretical Science (iTHES) Research Group, RIKEN, Wako, Saitama 351-0198, Japan*

⁵*Department of Physics, Toho University, Funabashi, Chiba 274-8510, Japan*

(Dated: May 10, 2018)

We perform a general-relativistic magnetohydrodynamics simulation for ≈ 30 ms from merger of a binary neutron star throughout the formation of a remnant massive neutron star (RMNS) with a high spatial resolution of the finest grid resolution 12.5 m. First, we show that the Kelvin-Helmholtz instability at merger could amplify the magnetic-field energy at least up to $\sim 1\%$ of the thermal energy. Then, we show that the magnetorotational instability in the RMNS envelope and torus with $\rho < 10^{13}$ g cm⁻³ sustains magneto-turbulent state and the effective viscous parameter in these regions is likely to converge to ≈ 0.01 – 0.02 with respect to the grid resolution. We also point out that the current grid resolution is not still fine enough to sustain magneto-turbulent state in the RMNS with $\rho \geq 10^{13}$ g cm⁻³.

PACS numbers: 04.25.D-, 04.30.-w, 04.40.Dg

I. INTRODUCTION

On August 17, 2017, the first direct detection of gravitational waves from a binary neutron star (BNS) merger GW170817 was achieved by Advanced LIGO and Advanced VIRGO [1]. Half a day after the gravitational wave event, electromagnetic emissions were observed in the UV-Optical-NIR bands [2–17], and it was concluded that these emissions named as AT2017gfo were associated with GW170817. Furthermore, a long-term monitoring of AT2017gfo in the X-ray and radio bands is being continued up to about 200 days after GW170817, and the observed emissions can be explained by synchrotron radiation associated with blast waves between the ejecta and interstellar medium [18–25].

The observed emissions in the UV-Optical-NIR bands are very consistent with the so-called kilonova/macronova model [26–28], and a significant amount of neutron-rich matter is likely to have been ejected during the merger. Recent numerical relativity simulations of the BNS mergers suggest that the mass ejection can be classified into two components: dynamical ejecta at the merger [29–37]; and post-merger ejecta from a merger remnant [38–50]. The dynamical ejecta are driven by tidal stripping of NSs and/or shock heating at a contact interface of two NSs. The post-merger ejecta from a merger remnant is driven by the angular momentum transport and the viscous heating due to effective turbulent viscosity [40, 47] (see also Refs. [39, 50] for the neutrino driven wind from the merger remnant). The effective viscosity is generated by magneto-turbulence inside the merger remnant, and the magneto-turbulent state is realized by several magnetohydrodynamical instabilities [51–63].

In particular, in the case of formation of a long-lived

remnant massive neutron star (RMNS), the post-merger ejecta could be a dominant component of the mass ejection from a BNS merger. The lifetime of the RMNS is determined by the total mass of BNSs, the equation of state (EOS), and the angular momentum transport process inside the RMNS. The observed total mass of GW170817 is between $\approx 2.73M_{\odot}$ and $\approx 2.78M_{\odot}$ [1] and this is consistent with the observed mass of binary pulsars [65]. In this event, the merger remnant is likely to collapse to a black hole within $O(10)$ s after the merger [38, 66, 67] because the formation of a permanently stable or very long-lived RMNS implies that additional energy injection due to the magnetic dipole radiation could occur and this is unlikely to be consistent with the electromagnetic emissions AT2017gfo [2–17]. On the other hand, if the total mass of BNSs is smaller than that of GW170817, a very long-lived RMNS could be formed. Indeed, very recently, a new BNS system PSR J1946+2052 was discovered, and its total mass is estimated as $2.50 \pm 0.04M_{\odot}$ [68]. Numerical relativity simulations in conjunction with these observational facts suggest that a bright electromagnetic counterpart to a gravitational-wave event which indicates the existence of a very long-lived RMNS could be observed in the near future [35, 70].

Thus, it is an urgent issue to investigate the mass ejection from very long-lived RMNSs for future observation. Because the post-merger mass ejection is driven primarily by the effective turbulent viscosity as mentioned above, general relativistic magnetohydrodynamics (GRMHD) simulation is an essential tool to explore the fate of the very long-lived RMNSs. In particular, the required grid resolution is high because the magneto-turbulence is easily killed by the large numerical diffusion for an insufficient grid resolution. However, it is computationally challenging to simulate entire evolution of the

RMNS for the viscous timescale while keeping such a high grid resolution.

We will tackle this problem step by step. As a first step, we read off the effective viscous parameter from a high-resolution GRMHD simulation of a BNS merger. As a second step, we will perform a long-term viscous hydrodynamics simulation with a hypothetical value of the viscous parameter which is suggested by the GRMHD simulation to explore the mass ejection and electromagnetic emission from the very long-lived RMNSs [40, 47, 48].

In this paper, we perform a high-resolution GRMHD simulation for a BNS merger and investigate to what extent the effective turbulent viscosity is generated inside the RMNSs. Specifically, we estimate the Shakura-Sunyaev α parameter and the convergence metrics which measure the sustainability of the magneto-turbulent state [88, 89]. In particular, we investigate the dependence of these quantities on the grid resolution by performing several simulations with different grid resolution. Finally, we discuss an implication to the value of the effective viscous parameter which is necessary for viscous hydrodynamics simulations.

This paper is organized as follows. In Sec. II, we describe our numerical method, grid setup, and initial condition. Section III presents simulation results. We provide discussions in Sec. IV and a summary in Sec. V.

II. METHOD, GRID SETUP, AND INITIAL MODELS

Our simulations are performed using a GRMHD code developed in Refs. [49, 55]. Einstein's equation is formulated in the framework of the puncture-Baumgarte-Shapiro-Shibata-Nakamura method [71–74]. Fourth-order finite differencing and lop-sided finite differencing for the advection terms are employed to discretize the field equations. GRMHD equations are formulated in a conservative form and solved by a high-resolution shock capturing scheme with a third-order reconstruction scheme [75]. We implement a fixed mesh refinement (FMR) algorithm together with the Balsara's method [76] to guarantee the divergence-free property of the magnetic field and magnetic flux conservation simultaneously.

In our FMR implementation, a simulation domain consists of several Cartesian boxes which have a common coordinate origin. The domain of each Cartesian refinement box is $x_l, y_l \in [-N\Delta x_l, N\Delta x_l]$, and $z_l \in [0, N\Delta x_l]$ where N is an integer and Δx_l is the grid spacing for the l -th refinement level. The relation between the grid spacing of coarser and finer refinement boxes is $\Delta x_{l-1} = 2\Delta x_l$ with $l = 2, 3, \dots, l_{\max}$. We impose the reflection symmetry across the orbital plane ($z = 0$). For the highest resolution run, we set $N = 702$, $l_{\max} = 10$, and $\Delta x_{10} = 50$ m until 5 ms before merger. With this setup, the volume of the largest refinement box is $\approx (35,900 \text{ km})^3/2$. Subsequently, we apply a prescription in Ref. [56] to improve

the grid resolution in the central region. Specifically, we generate two *new* finer FMR boxes of $\Delta x_{11} = 25$ m and $\Delta x_{12} = 12.5$ m while keeping the grid number N . With this setting, we performed simulations up to about 30 ms after merger using 32,000 cores on the Japanese K computer. The simulation cost is about 40 million core hours. To investigate numerical convergence, we also performed a middle resolution run with $N = 482$, $l_{\max} = 10$, and $\Delta x_{10} = 70$ m and a low resolution run with $N = 312$, $l_{\max} = 10$, and $\Delta x_{10} = 110$ m. During these simulations, we did not improve the resolution in the central region.

We employ a BNS in a quasi-circular orbit with mass $1.25M_\odot$ – $1.25M_\odot$ as initial data. This NS mass is close to the lower end of the observed NS mass in the BNS systems, PSR J1946+2052 [68]. The initial orbital angular velocity is $Gm_0\Omega/c^3 = 0.0221$, where $m_0 = 2.5M_\odot$, G is the gravitational constant, and c is the speed of light. We adopt the H4 EOS [77] to model the NS with which the maximum mass of a cold spherical NS is $\approx 2.03M_\odot$. For the numerical evolution of the system, a piecewise polytrope prescription [78] is employed to model the cold part of the EOS. The thermal part of the EOS is written in a Γ -law form with $\Gamma = 1.8$ [29].

Following Ref. [55], we set the vector potential of the initial magnetic field in the form

$$A_i = [-(y - y_{\text{NS}})\delta_i^x + (x - x_{\text{NS}})\delta_i^y]A_b \max(P - P_c, 0)^2, \quad (2.1)$$

where x_{NS} and y_{NS} denote the coordinate center of the NS. P is the pressure and P_c is a cutoff value, which we set to be the value of the pressure at 4% of the maximum rest-mass density. A_b is a constant which determines the amplitude of the magnetic field and we set the initial maximum magnetic-field strength to be 10^{15} G. This initial magnetic-field strength is justified by our recent study [56]: We have already found that a moderately weak initial magnetic field of 10^{13} G is amplified to $\gtrsim 10^{15.5}$ – 10^{16} G by the Kelvin-Helmholtz instability only within a few milliseconds after the onset of merger, and thus, the final value of the magnetic-field strength depends very weakly on the initial value [79].

III. RESULTS

A. Dynamics

We start the simulation from an inspiral part of about 5 orbits before the onset of merger. After merger, a RMNS is formed. Employing the nuclear-theory-based neutron-star EOS, the maximum mass of cold rigidly-rotating NSs is by $\approx 20\%$ larger than that of cold spherical NSs [80], which is $2.03M_\odot$ for the present model. During the merger, the material is shock-heated and the temperature of the RMNS is increased to several tens of MeV. Then, the resultant thermal pressure provides additional force to support the self-gravity of the RMNS [81]. This effect increases the maximum mass by several percents [81, 82].

With these effects, the maximum mass of the hot and rigidly rotating NS with the H4 EOS is greater than $\approx 2.44M_{\odot}$ [83]. Because the gravitational wave energy emitted during the inspiral and merger phases is $\approx 2.2\%$ of the initial gravitational mass, the gravitational mass of the RMNS is smaller than $2.44M_{\odot}$. Thus, such a RMNS should survive for a timescale of neutrino cooling or for that of dissipation of angular momentum by, e.g., magnetic dipole radiation.

Figure 1 plots profiles of the rest-mass density (panels a1–a4), the magnetic-field strength (panels b1–b4), the plasma beta defined by $\beta \equiv P/P_{\text{mag}}$ (panels c1–c4), and the angular velocity (panels d1–d4) on a meridional plane at different time slices after merger. Here P_{mag} is magnetic pressure. The merger time t_{merger} is defined as the time at which the amplitude of gravitational waves achieves its maximum (see also the visualization in Ref. [87]). The merger remnant is composed of a dense RMNS surrounded by a massive torus. We define the RMNS and its core by fluid elements with rest-mass density $\rho \geq 10^{13} \text{g cm}^{-3}$ and $\rho \geq 10^{14} \text{g cm}^{-3}$, respectively. The RMNS has a highly flattened structure due to the rapid and differential rotation, as shown in Fig. 1 (panel a1). The matter with $\rho \leq 10^{13} \text{g cm}^{-3}$ constitutes a torus and envelope. Thermal pressure and centrifugal force push the fluid elements outward. Due to torque exerted by the non-axisymmetric structure of the rest-mass density of the RMNS, the angular momentum is transported outward. Consequently, the torus gradually expands quasi-radially as shown in Fig. 1 (panels a2–a4).

In the early stage of merger, the magnetic field is steeply amplified and a strongly magnetized RMNS is formed as shown in Fig. 1 (panel b1). The magnetic-field amplification is caused primarily by the Kelvin-Helmholtz instability that is developed in shear layers. The shear layer first emerges when the two NSs come into contact. It is reinforced whenever the two dense cores formed after merger collide until they settle to a single core [55, 56]. The magnetic field is also amplified in the outer envelope by MRI (panels b2–b4). Note that the growth rate of the Kelvin-Helmholtz instability is proportional to the wavenumber, i.e., small-scale vortices grow faster than large-scale vortices. Therefore, even the 12.5 m run does not fully capture the growth of the magnetic field. We analyze the magnetic-field amplification due to the Kelvin-Helmholtz instability and MRI in Secs. III B and III C.

Figure 1 (c1–c4) plots the plasma beta on a meridional plane. These panels show that the matter pressure dominates the magnetic-field pressure in both RMNS and its envelope. This indicates that the force-free magnetic field is not developed in the RMNS envelope at this moment. Note that the plasma beta in the RMNS core may be smaller in reality than that found in this study because the Kelvin-Helmholtz instability could further amplify the magnetic field.

The RMNS settles to a quasi-stationary state at 13–15 ms after merger (panels d1–d2 of Fig. 1 and see also

Fig. 2). The angular velocity deep inside the RMNS core is smaller than that of the RMNS core surface in our numerical result [84]. Thus, the radial profile of the angular velocity has an off-center peak (panels d3–d4 of Fig. 1). The reason for this is that at the collision of two NSs, the kinetic energy is dissipated at the contact interface (but see a discussion below). Figure 2 shows spacetime diagrams of the rest-mass density and the angular velocity on the orbital plane for three different grid resolutions. We average both profiles along the azimuthal direction. The off-center peak of the angular velocity profile appears at $r \approx 10$ km for $t - t_{\text{merger}} \gtrsim 13$ –15 ms. This figure also shows that the angular velocity around the center is damped for $t - t_{\text{merger}} \lesssim 12$ –14 ms for the 12.5 m and 70 m runs. The damping is seen for $t - t_{\text{merger}} \lesssim 5$ –6 ms for the 110 m run. Note that the quick damping of the angular velocity around the center may not be conclusive because our simulation is not convergent for resolving the Kelvin-Helmholtz instability (see also Fig. 8 for the convergence in the power spectrum.) However, we may conclude that irrespective of the grid resolution the region with $\rho \lesssim 10^{14-14.5} \text{g cm}^{-3}$ inside the RMNS is subject to the MRI [51, 52], because of its extremely rapid and strongly-differential rotation with negative radial gradient of the angular velocity. On the other hand, the angular velocity profile inside the RMNS core depends significantly on the grid resolution. If we believe the results in the highest-resolution run, the region with $\rho \gtrsim 10^{14-14.5} \text{g cm}^{-3}$ is not likely to be subject to the MRI. However in the presence of a highly developed poloidal magnetic field in a differentially rotating medium, an efficient angular momentum transport could work by magnetic winding and associated magnetic braking [86].

Figure 3 plots the radial profiles of the rest-mass density and the angular velocity on the orbital plane for all the runs at $t - t_{\text{merger}} = 15$ ms and 30 ms. As in Fig. 2, we average the profiles along the azimuthal direction. The rest-mass density profiles depend weakly on the grid resolution. The off-center peak of the angular velocity is located at $R = 9$ –10 km and its position does not change significantly during the simulation. However, this result is not still conclusive because in the central region, the angular velocity exhibits dependence on the grid resolution. The profiles with $R \gtrsim 15$ km are not likely to depend significantly on the grid resolution.

Figure 4 plots the evolution of the magnetic-field energy, the rotational kinetic energy and the internal energy. The solid and dashed curves in the left panel correspond to poloidal and toroidal components, respectively. Both components are amplified exponentially in the early stage of merger and saturate eventually. Here, the time of the saturation depends on the grid resolution. This exponential growth is initiated by the Kelvin-Helmholtz instability [56]. There is no prominent growth of the magnetic-field energy after the saturation. For the 70 m and 110 m runs, the rapid growth of the magnetic-field energy due to the Kelvin-Helmholtz instability becomes

less prominent and it is found that the toroidal magnetic-field energy is amplified for $t - t_{\text{merger}} \gtrsim 10$ ms due to the magnetic winding and MRI. This feature is obviously unphysical because in reality, the magnetic-field energy is steeply increased by the Kelvin-Helmholtz instability until the saturation is reached.

The middle and right panels of Fig. 4 show that the rotational kinetic energy is $\approx 10^{53}$ erg and the internal energy is $\approx 2.6 \times 10^{53}$ erg at $t - t_{\text{merger}} \approx 30$ ms for the highest resolution run. Because both energies are larger than the magnetic-field energy, the saturation energy of the magnetic field could be larger than that found in the current work. We expect that the magnetic-field energy could increase up to $\sim 10^{51}$ erg in reality as discussed in Sec. IV.

B. Tomography of magnetic-field amplification

Because of a highly dynamical situation, it is not trivial to disentangle the amplification due to the Kelvin-Helmholtz instability, the MRI, and magnetic winding. Therefore, we perform a detailed analysis for the magnetic-field amplification in this section. First, we foliate the RMNS and its envelope in terms of the rest-mass density and estimate a volume average defined by

$$\langle q \rangle_a = \frac{\int_{V_a} q d^3x}{\int_{V_a} d^3x} \quad (3.1)$$

where V_a denotes a region with $a \leq \log_{10}[\rho \text{ (g cm}^{-3}\text{)}] < a+1$ and q is any physical quantity such as the magnetic-field component and the rest-mass density. In this subsection, we choose $q = b_i$ with $i = R, \varphi$ where b_i is a spatial component of magnetic field measured in the fluid rest frame. Figure 5 plots $\langle b_R \rangle$ and $\langle b_\varphi \rangle$ as functions of time for all the runs with $a = 10\text{--}14$.

We first describe our finding for the results of the 12.5 m run. Irrespective of choice of the density range, both components exhibit a prominent growth in the early stage of merger due to the Kelvin-Helmholtz instability for $t - t_{\text{merger}} \lesssim 3\text{--}4$ ms at which the exponential growth of the magnetic-field energy is saturated in the high-density range with $a = 12\text{--}14$. After the saturation is reached, there is no prominent growth of the magnetic field in these density ranges. On the other hand, in the low-density region with $a = 10$ and 11 the exponential growth is still seen for $t - t_{\text{merger}} \lesssim 6\text{--}7$ ms. The growth rate of the poloidal magnetic-field strength is $\approx 1400 \text{ s}^{-1}$ for $4 \lesssim t - t_{\text{merger}} \lesssim 5$ ms with $a = 11$. For the relatively low-density region with $\rho \lesssim 10^{12} \text{ g cm}^{-3}$, the fastest growing mode of the MRI is covered by more than 10 grid points (see Fig. 6).

For the 70 m and 110 m runs, the magnetic-field amplification for $t - t_{\text{merger}} \lesssim 4\text{--}5$ ms is less prominent compared to that for the 12.5 m run irrespec-

tive of the density range. After this early amplification phase, the toroidal component is amplified for the 70 m and 110 m runs in the density range with $a = 11\text{--}14$. This is due to the magnetic winding and the non-axisymmetric MRI [55]. Note that the fastest growing mode of the non-axisymmetric MRI is covered by more than 10 grid points in both 70 m and 110 m runs for $\rho < 10^{13} \text{ g cm}^{-3}$ as we discuss in the next subsection (see also Table I). However, the amplification due to the winding and non-axisymmetric MRI found in the low resolution runs is unphysical because this tomography suggests that the magnetic-field energy would saturate within a short timescale after merger in all the density ranges due to the Kelvin-Helmholtz instability and the MRI.

Because the MRI in combination with the Kelvin-Helmholtz instability develops in the RMNS and its envelope and subsequently it drives magneto-turbulence, the resultant effective turbulent viscosity should transport angular momentum outward [51, 52]. In Sec. IIID, we analyze angular momentum transport due to the MRI-driven turbulence in detail.

C. MRI-driven turbulence

After the saturation of the magnetic-field growth, the MHD-driven turbulence is likely to be developed. In the presence of a region of $\partial\Omega/\partial R < 0$, MRI plays a role for sustaining the MHD-driven turbulence. Following Refs. [88, 89], we here evaluate the convergence metrics to investigate the sustainability of the MRI-driven turbulence:

$$Q_z = \frac{\lambda_{\text{MRI}}^z}{\Delta x_l}, \quad (3.2)$$

$$Q_\varphi = \frac{\lambda_{\text{MRI}}^\varphi}{\Delta x_l}, \quad (3.3)$$

$$\mathcal{R} = \frac{b_R^2}{b_\varphi^2}. \quad (3.4)$$

and

$$\alpha_{\text{mag}} = \frac{W_{R\varphi}}{b^2/8\pi}. \quad (3.5)$$

We estimate the wavelength of the fastest growing mode of the MRI as

$$\lambda_{\text{MRI}}^i = \frac{b_i}{\sqrt{4\pi\rho h + b^2}} \frac{2\pi c}{\Omega} \quad (i = z \text{ or } \varphi), \quad (3.6)$$

where h is the relativistic specific enthalpy and $b^2 = b^\mu b_\mu$. b^μ is the magnetic field measured in the fluid rest frame. $W_{R\varphi}$ is the Maxwell stress defined by

$$W_{R\varphi} = - \left\langle \frac{b_R b_\varphi}{4\pi} \right\rangle_T. \quad (3.7)$$

$\langle \cdot \rangle_T$ denotes a time average over 1 ms at each location.

We again foliate the RMNS and its envelope in terms of the rest-mass density and estimate volume-averaged convergence metrics defined by Eq. (3.1). Comparison of the global simulations with local box simulations for Newtonian accretion-disk systems suggests that $\langle Q_z \rangle \gtrsim 15$, $\langle Q_\varphi \rangle \gtrsim 20$, $\langle \mathcal{R} \rangle \gtrsim 0.2$, and $\langle \alpha_{\text{mag}} \rangle \gtrsim 0.45$ are necessary to sustain the MRI-driven turbulence [88, 89]. Q_z and Q_φ measure how many grid points are assigned for resolving the MRI wavelength of the fastest growing mode. α_{mag} is similar to the α parameter, but it is defined only by the magnetic-field component in the stress tensor. This quantity measures the correlation between the radial and azimuthal components of the magnetic field. \mathcal{R} measures the capability to generate the poloidal field due to the nonlinear development of the MRI-driven turbulence.

Figure 6 shows $\langle Q_z \rangle_a$, $\langle \mathcal{R} \rangle_a \equiv \langle b_R^2/b_\varphi^2 \rangle_a$, and $\langle \alpha_{\text{mag}} \rangle_a$ as functions of time for $a = 10$ –14. Because $\langle Q_\varphi \rangle_a$ is always larger than $\langle Q_z \rangle_a$, we do not show the evolution of $\langle Q_\varphi \rangle_a$. For $a = 14$, $\langle Q_z \rangle$ satisfies the criterion for the 12.5 m run and does not for either 70 m nor 110 m runs. $\langle \mathcal{R} \rangle$ decreases with time irrespective of the grid resolution and reaches a value below the criterion. Note the RMNS is in a highly dynamical state for $t - t_{\text{merger}} \lesssim 13$ –15 ms (see Fig. 2). $\langle \alpha_{\text{mag}} \rangle$ is always below the criterion irrespective of the grid resolution. However, this is a natural consequence because most part of this density region (in our simulation results) is not subject to the MRI as discussed in the previous subsection. We note that as already mentioned in Sec. III A, for a high-density range with $\rho \gtrsim 10^{14}$ g cm $^{-3}$, we have not yet obtained a convergent result. In the assumption that the results in our current best-resolution runs are not far from the convergence, we may conclude not the MRI but the winding due to the strong poloidal field is likely to play a dominant role in the angular momentum transport. However, we need to keep in mind that a more resolved study is required for clarifying the turbulent state of the high-density region.

For $a = 13$, $\langle Q_z \rangle$ is larger than the criterion for the 12.5 m run and far below the criterion for the 70 m and 110 m runs. $\langle \mathcal{R} \rangle$ decreases with time and reaches below the criterion. Even for the 12.5 m run, this convergence metric approaches ≈ 0.1 at $t - t_{\text{merger}} \approx 30$ ms. This asymptotic value is increased with improving the grid resolution. $\langle \alpha_{\text{mag}} \rangle$ is smaller than the criterion for all the runs. Thus, convergence is not achieved even for the 12.5 m run. However, the time-averaged value of this convergence metric is increased with improving the grid resolution (see Table I). This suggests that the sustainability of the MRI-driven turbulence is improved with the grid resolution and the magneto-turbulent state may be partially sustained for the 12.5 m run.

For $a = 12$, $\langle Q_z \rangle$ is larger than the criterion for the 12.5 m and 70 m runs. It is smaller than the criterion for the 110 m run. A mean value of $\langle \mathcal{R} \rangle$ with respect to the time is ≈ 0.2 for the 12.5 m and 70 m runs (thus, the criterion to sustain the turbulence is marginally satisfied), but it is

much smaller than 0.2 for the 110 m run for $t - t_{\text{merger}} \gtrsim 15$ ms. $\langle \alpha_{\text{mag}} \rangle$ fluctuates around 0.52 for the 12.5 m and 70 m runs. Therefore, the magneto-turbulence is sustained in these runs. For the 110 m run, $\langle \alpha_{\text{mag}} \rangle$ starts decreasing at $t - t_{\text{merger}} \approx 17$ –18 ms and reaches a value below the criterion. This might be ascribed to numerical resistivity because the low value of $\langle Q_z \rangle$ suggests that the MRI is not developed for the 110 m run. On the other hand, the 12.5 m and 70 m runs likely have the capability to sustain the MRI-driven turbulence in this density range.

For $a = 11$, $\langle Q_z \rangle$ satisfies the criterion at $t - t_{\text{merger}} \gtrsim 10$ ms irrespective of the grid resolution. The asymptotic value of $\langle \mathcal{R} \rangle$ with respect to the time is ≈ 0.17 for the 12.5 m run, ≈ 0.15 for the 70 m run, and ≈ 0.12 for the 110 m run. Therefore, the criterion is approximately satisfied because the value is close to 0.2. Irrespective of the grid resolution, $\langle \alpha_{\text{mag}} \rangle$ is larger than the criterion. We find a similar trend in the convergence metrics for $a = 10$ although $\langle \alpha_{\text{mag}} \rangle$ is slightly smaller than the criterion. This indicates that the MRI-driven turbulence is marginally sustained in these low-density regions irrespective of the grid resolution.

We take the following time-average of the volume-averaged convergence metrics for $15 \text{ ms} \leq t - t_{\text{merger}} \leq 30$ ms in each density range and summarize in Table I;

$$\langle \langle q \rangle \rangle_a = \frac{1}{T} \int_{15\text{ms}}^{30\text{ms}} \langle q \rangle_a dt, \quad (3.8)$$

with $T = 15$ ms. We choose this time window because the RMNS settles to a quasi-stationary state for $t - t_{\text{merger}} \gtrsim 15$ ms as shown in Fig. 2. Table I shows that the convergence metrics in a region with $\rho < 10^{13}$ g cm $^{-3}$ is likely to satisfy the criterion [88, 89] for the 12.5 m and 70 m runs. For the 110 m run, the MRI-driven turbulence is decayed by the large numerical diffusion due to the insufficient grid resolution. In the high-density range with $\rho \geq 10^{13}$ g cm $^{-3}$, all the convergence metrics increase with improving the grid resolution. This indicates that the MRI cannot be fully resolved and the MRI-driven turbulence still suffers from the numerical diffusion even for the highest resolution run.

D. Effective α parameter and angular momentum transport timescale

We evaluate an effective α -viscosity parameter defined by

$$\alpha = \frac{1}{\langle P \rangle_T} \left\langle \rho \delta v^R \delta v^\varphi - \frac{b_R b_\varphi}{4\pi} \right\rangle_T, \quad (3.9)$$

where $\delta v^i = v^i - \langle v^i \rangle_T$ is the velocity fluctuation in time [88]. Again, $\langle \cdot \rangle_T$ denotes a time average over 1 ms. Figure 7 shows the time evolution of the volume-averaged values, $\langle \alpha \rangle_a$, with $a = 10$ –14. Table I summarizes the values of $\langle \langle \alpha \rangle \rangle$.

For $a = 14$, the α parameter is $O(10^{-4})$ for $t - t_{\text{merger}} \gtrsim 15$ ms. A possible reason for this small value is that this high-density region (i.e., central region of the RMNS) might not be subject to the MRI. However for the high-density region, our simulation cannot fully resolve the Kelvin-Helmholtz instability and we cannot draw a definite conclusion.

For $a = 13$ (i.e., for the outer region of the RMNS) for which the MRI should play a key role for the angular momentum transport, the mean value of the α parameter with respect to the time is $\approx 5 \times 10^{-3}$ for the 12.5 m run, $\approx 3 \times 10^{-3}$ for the 70 m run, and $\approx 2 \times 10^{-3}$ for the 110 m run. Thus, the value increases with improving the grid resolution (see also Table I) and hence α is likely to be larger than this value in reality.

For $a = 12$, the time evolution curves of the α parameter approximately overlap for the 12.5 m and 70 m runs for $t - t_{\text{merger}} \gtrsim 15$ ms and the mean values with respect to the time is $\approx 0.01 - 0.02$ for these runs. The α parameter for the 110 m run is always smaller than those for the higher resolution runs. Note that dependence of the convergence metrics \mathcal{R} and α_{mag} on the grid resolution exhibits a similar trend as discussed in the previous subsection. For $a = 11$ and 10, the evolution feature and the dependence on the grid resolution of the α parameters are similar to those for $a = 12$ [92].

Because the α parameter as well as the convergence metrics in the RMNS tends to increase with improving the grid resolution, we conclude that the MRI-driven turbulence is not fully sustained even for the highest resolution run resulting in underestimate of the effective viscosity. Therefore, the α parameter of the RMNS derived in this work should be regarded as a lower limit.

For the envelope, the detailed analysis of the convergence metrics indicates that the grid resolution with $\Delta x \lesssim 70$ m has a capability to sustain the MRI-driven turbulence and the resultant effective viscosity parameter is $\approx 0.01 - 0.02$. These values of the α parameter and the convergence metrics discussed above are consistent with those in the local shearing box simulations [88].

We estimate the angular momentum transport timescale by the shear viscous effect by $j/(\alpha c_s^2)$ [53]. Table II shows the estimated viscous timescale in each density range. Note that the viscous timescale of the RMNS ($a = 13$) is longer than that of the envelope ($a = 12, 11$) because the α parameter would be underestimated inside the RMNS due to the limitation of the grid resolution as discussed above. On the other hand, the α parameter of the envelope is not likely to depend significantly on the grid resolution. For $a = 14$, the viscous timescale is shorter than that for $a = 13$ even though the α parameter is much smaller than that for $a = 13$ (see Table I). This is because the specific angular momentum is small and the sound speed is high. As we discuss in Sec. IV, the magnetic braking associated with the magnetic winding could play a role for the angular momentum redistribution in this high-density region.

E. Power spectrum of magnetic field

Figure 8 plots the power spectrum of the poloidal magnetic-field energy. To calculate the power spectrum, we first define the Fourier component of the poloidal magnetic-field strength by

$$\tilde{b}_p(\vec{k}) \equiv \iiint b_p(\vec{x}) e^{-i\vec{k}\cdot\vec{x}} d^3x, \quad (3.10)$$

where $\vec{k} = (k_x, k_y, k_z)$, $\vec{x} = (x, y, z)$, and $b_p^2 = b_R^2 + b_z^2$. Then, we define the power spectrum of the poloidal magnetic-field energy by

$$P_B(k) \equiv \frac{1}{(2\pi)^3} \int \frac{1}{8\pi} \tilde{b}_p(\vec{k}) \tilde{b}_p^*(\vec{k}) k^2 d\Omega_k, \quad (3.11)$$

where \tilde{b}_p^* is a complex conjugate of \tilde{b}_p , $k = |\vec{k}|$, and $d\Omega_k$ is a solid angle in the k -space. Integration of the power spectrum with respect to k gives the poloidal magnetic-field energy. Figure 8 shows the power spectrum, $kP_B(k)$, at $t - t_{\text{merger}} = 1$ ms, 15 ms, and 30 ms. Because of the Kelvin-Helmholtz instability, the power spectrum amplitude at $t - t_{\text{merger}} = 1$ ms for the 12.5 m run is much larger than those for the 70 and 110 m runs. This feature is remarkable at high wavenumber, i.e., at small scale. The amplitude for the 12.5 m run is larger than those for the 70 m and 110 m run because the kinetic energy of the turbulence is converted to the magnetic-field energy more efficiently in the higher resolution runs [56]. However even for the 12.5 m run we do not obtain the convergence for the magnetic-field amplification due to the Kelvin-Helmholtz instability because the saturated magnetic-field energy is much smaller than the rotational kinetic and internal energy as discussed in Sec. III A.

The spectrum amplitude at low wavenumber $k \lesssim 10^{-6} \text{ cm}^{-1}$ increases from $t - t_{\text{merger}} = 1$ ms to 15 ms, which may indicate inverse cascade due to the MRI [53]. The spectrum is flat in the inertial range of the turbulent cascade, $10^{-6} \lesssim k [\text{cm}^{-1}] \lesssim 10^{-4}$ for the highest resolution run, which is likely to be consistent with a feature found in the local simulations of a large-scale dynamo during the kinematical amplification phase [90].

Note that a coherent large-scale magnetic field such as a dipole field is not developed during the simulation time although small-scale magnetic fields are amplified by the Kelvin-Helmholtz instability and the MRI. One possibility is that the grid resolution in this work is still insufficient to simulate a large-scale dynamo (see Ref. [91] for the large-scale dynamo of the toroidal magnetic field). The other possibility is that a part of the dynamical ejecta falls back onto the RMNS and the matter inertia still dominates the electromagnetic force around the RMNS as shown in Fig. 1 (c1-c4). Therefore, the magnetic pressure alone cannot drive an outflow and this indicates the formation of the coherent poloidal magnetic field in the early time of $\lesssim 30$ ms is unlikely.

TABLE I. Time- and volume-averaged convergence metrics Q_z , Q_φ , \mathcal{R} , and α_{mag} . The time average is carried out for $15 \text{ ms} \leq t - t_{\text{merger}} \leq 30 \text{ ms}$. We show the result for three different grid resolutions. The criterion for the sustainability of the MRI-driven turbulence is given by $\langle Q_z \rangle \gtrsim 15$, $\langle Q_\varphi \rangle \gtrsim 20$, $\langle \mathcal{R} \rangle \gtrsim 0.2$, and $\langle \alpha_{\text{mag}} \rangle \gtrsim 0.45$, respectively. Note that in the low-density ranges with $a = 11$ and 10 the grid resolution for the highest resolution run is improved by only a factor of 1.4 and 2.2 compared to the middle and low resolution runs, respectively because of our choice of the grid structure in the FMR algorithm. This results in a moderate improvement of $\langle Q_z \rangle$ in these density ranges compared to the high-density ranges with $a = 12-14$.

$\Delta x_{t_{\text{max}}} [\text{m}]$	$\langle\langle Q_z \rangle\rangle_{14}$	$\langle\langle Q_z \rangle\rangle_{13}$	$\langle\langle Q_z \rangle\rangle_{12}$	$\langle\langle Q_z \rangle\rangle_{11}$	$\langle\langle Q_z \rangle\rangle_{10}$
12.5	72.3	44.5	52.3	57.5	64.4
70	2.2	3.4	25.1	36.2	37.1
110	0.8	0.5	8.9	17.9	15.4
$\Delta x_{t_{\text{max}}} [\text{m}]$	$\langle\langle Q_\varphi \rangle\rangle_{14}$	$\langle\langle Q_\varphi \rangle\rangle_{13}$	$\langle\langle Q_\varphi \rangle\rangle_{12}$	$\langle\langle Q_\varphi \rangle\rangle_{11}$	$\langle\langle Q_\varphi \rangle\rangle_{10}$
12.5	751.1	668.0	594.1	716.8	560.0
70	37.6	55.4	229.0	438.2	377.0
110	20.1	21.8	106.1	237.0	141.3
$\Delta x_{t_{\text{max}}} [\text{m}]$	$\langle\langle \mathcal{R} \rangle\rangle_{14}$	$\langle\langle \mathcal{R} \rangle\rangle_{13}$	$\langle\langle \mathcal{R} \rangle\rangle_{12}$	$\langle\langle \mathcal{R} \rangle\rangle_{11}$	$\langle\langle \mathcal{R} \rangle\rangle_{10}$
12.5	0.20	0.16	0.24	0.26	0.26
70	0.10	0.10	0.24	0.23	0.20
110	0.06	0.05	0.13	0.18	0.19
$\Delta x_{t_{\text{max}}} [\text{m}]$	$\langle\langle \alpha_{\text{mag}} \rangle\rangle_{14}$	$\langle\langle \alpha_{\text{mag}} \rangle\rangle_{13}$	$\langle\langle \alpha_{\text{mag}} \rangle\rangle_{12}$	$\langle\langle \alpha_{\text{mag}} \rangle\rangle_{11}$	$\langle\langle \alpha_{\text{mag}} \rangle\rangle_{10}$
12.5	-0.03	0.34	0.52	0.49	0.40
70	-0.11	0.25	0.53	0.49	0.41
110	-0.18	0.14	0.43	0.47	0.38
$\Delta x_{t_{\text{max}}} [\text{m}]$	$\langle\langle \alpha \rangle\rangle_{14}$	$\langle\langle \alpha \rangle\rangle_{13}$	$\langle\langle \alpha \rangle\rangle_{12}$	$\langle\langle \alpha \rangle\rangle_{11}$	$\langle\langle \alpha \rangle\rangle_{10}$
12.5	0.0005	0.005	0.017	0.012	0.005
70	0.0002	0.003	0.017	0.012	0.005
110	0.0004	0.002	0.010	0.010	0.003

TABLE II. Volume- and time-averaged specific angular momentum, the sound speed, and viscous timescale for $15 \text{ ms} \leq t - t_{\text{merger}} \leq 30 \text{ ms}$ with the highest resolution run. The parenthesis of the viscous timescale for $a = 13$ and $a = 14$ implies that it should be shorter in reality because we underestimate the α parameter.

$\langle\langle j \rangle\rangle_{14} [\text{cm}^2 \text{ s}^{-1}]$	$\langle\langle j \rangle\rangle_{13} [\text{cm}^2 \text{ s}^{-1}]$	$\langle\langle j \rangle\rangle_{12} [\text{cm}^2 \text{ s}^{-1}]$	$\langle\langle j \rangle\rangle_{11} [\text{cm}^2 \text{ s}^{-1}]$	$\langle\langle j \rangle\rangle_{10} [\text{cm}^2 \text{ s}^{-1}]$
0.78×10^{16}	2.51×10^{16}	3.16×10^{16}	3.38×10^{16}	3.76×10^{16}
$\langle\langle c_s \rangle\rangle_{14} [\text{c}]$	$\langle\langle c_s \rangle\rangle_{13} [\text{c}]$	$\langle\langle c_s \rangle\rangle_{12} [\text{c}]$	$\langle\langle c_s \rangle\rangle_{11} [\text{c}]$	$\langle\langle c_s \rangle\rangle_{10} [\text{c}]$
0.33	0.13	0.14	0.10	0.06
$\langle\langle t_{\text{vis}} \rangle\rangle_{14} [\text{s}]$	$\langle\langle t_{\text{vis}} \rangle\rangle_{13} [\text{s}]$	$\langle\langle t_{\text{vis}} \rangle\rangle_{12} [\text{s}]$	$\langle\langle t_{\text{vis}} \rangle\rangle_{11} [\text{s}]$	$\langle\langle t_{\text{vis}} \rangle\rangle_{10} [\text{s}]$
(< 0.16)	(< 0.33)	0.11	0.27	2.32

IV. DISCUSSION

A. Inferred value of the saturated magnetic-field energy and α parameter in the core region

Because the viscous parameter as well as the convergence metrics in the RMNS core exhibit strong dependence on the grid resolution, we were not able to obtain the convergent values of these quantities. In the following, we infer the convergent values for the core region by extrapolating from the simulation data in the envelope region in which the result does not depend significantly on the grid resolution.

Figure 9 plots volume-averaged Alfvén velocity nor-

malized by the sound speed as a function of time in each density range. We show both radial and azimuthal components of the Alfvén velocity:

$$v_{A,i} \equiv \frac{b_i}{\sqrt{4\pi\rho h + b^2}} c \quad (i = R \text{ or } \varphi). \quad (4.1)$$

For $a \leq 12$, $\langle v_{A,R}/c_s \rangle$ and $\langle v_{A,\varphi}/c_s \rangle$ converge at 0.03–0.04 and 0.08–0.09, respectively. By contrast, for $a \geq 13$, both quantities are far from the convergence. We extrapolate the toroidal magnetic-field strength in the

high-density region from the results with $a \leq 12$ as

$$b_\varphi \sim \sqrt{4\pi\rho}v_{A,\varphi} \sim 10^{17} \left(\frac{c_s}{0.3c}\right) \left(\frac{\rho}{10^{15}\text{g cm}^{-3}}\right)^{1/2} \text{G} \quad (4.2)$$

with $v_{A,\varphi} \sim 0.1c_s$. The poloidal magnetic-field strength in the high-density region is expected to be

$$b_R \sim \frac{1}{3}b_\varphi \sim 3 \times 10^{16} \left(\frac{c_s}{0.3c}\right) \left(\frac{\rho}{10^{15}\text{g cm}^{-3}}\right)^{1/2} \text{G}. \quad (4.3)$$

This estimation suggests that in reality the toroidal magnetic field in the core region of the RMNS might be further amplified by a factor of ~ 3 – 4 which results in $E_B \sim 10^{51}$ erg. This energy is $\sim 1\%$ of E_{rot} and E_{int} .

Figure 10 plots the time- and volume-averaged α parameter as a function of $\mathcal{M} \equiv \langle v_{A,R}/c_s \rangle_a \langle v_{A,\varphi}/c_s \rangle_a$ for $a = 11$ – 14 . We show the results for the 12.5 m and 70 m runs. For $a = 12$ and 11, the α parameter converges to 0.01–0.02 at $\mathcal{M} \approx 0.003$. If we extrapolate the α parameter for $a = 13$ with respect to \mathcal{M} , it should be ~ 0.01 – 0.02 . Consequently, we get

$$t_{\text{vis},13} \approx 83 \text{ ms} \left(\frac{\langle\langle\alpha\rangle\rangle_{13}}{0.02}\right)^{-1} \left(\frac{\langle\langle j \rangle\rangle_{13}}{2.5 \times 10^{16} \text{ cm}^2 \text{ s}^{-1}}\right) \times \left(\frac{\langle\langle c_s \rangle\rangle_{13}}{0.13c}\right)^{-2}, \quad (4.4)$$

where $\langle\langle j \rangle\rangle_a$ and $\langle\langle c_s \rangle\rangle_a$ with $a = 13$ are time- and volume-averaged specific angular momentum and the sound speed in the RMNS for the 12.5 m run with $15 \leq t - t_{\text{merger}} \leq 30$ ms, respectively (see Table II).

Because the α parameter in the density range with $a = 14$ is far from the convergence, it is difficult to extrapolate with respect to \mathcal{M} . Nonetheless, speculating that the α parameter in the density range with $a = 14$ would be 0.01–0.02 because the feature of the magneto-turbulence may be similar inside the envelope and the core, the viscous timescale in this high-density region would be

$$t_{\text{vis},14} \approx 4 \text{ ms} \left(\frac{\langle\langle\alpha\rangle\rangle_{14}}{0.02}\right)^{-1} \left(\frac{\langle\langle j \rangle\rangle_{14}}{7.8 \times 10^{15} \text{ cm}^2 \text{ s}^{-1}}\right) \times \left(\frac{\langle\langle c_s \rangle\rangle_{14}}{0.33c}\right)^{-2}, \quad (4.5)$$

Therefore according to the estimation of the viscous timescale Eqs. (4.4) or (4.5), we speculate that the RMNS gradually approaches a rigid-rotation state within this viscous timescale.

B. Magnetic winding and braking in the high-density region

Our current results show that for the region with $\rho \gtrsim 10^{14} \text{ g cm}^{-3}$, the radial gradient of the angular ve-

locity is positive as shown in Figs. 2 and 3. The magnetic winding would work in this high-density region even though the MRI might not turn on and the magnetic braking timescale is estimated to give

$$t_{\text{brake}} = \frac{R}{v_{A,R}} \approx 5 \text{ ms} \left(\frac{b_R}{3 \times 10^{16} \text{ G}}\right)^{-1} \left(\frac{\rho}{10^{15} \text{ g cm}^{-3}}\right)^{1/2} \times \left(\frac{R}{15 \text{ km}}\right).$$

Because there is a room for the magnetic-field amplification due to the Kelvin-Helmholtz instability as discussed in Sec. III B, the braking timescale could be shorter than 5 ms in reality. However note that the coherent poloidal field is assumed to be developed for this estimation.

For the small-scale randomly-oriented magnetic fields like those found in this study, the braking timescale may be written as

$$t_{\text{brake}} = \frac{R}{v_{A,R}} \left(\frac{R}{\delta R}\right) \approx 750 \text{ ms} \left(\frac{b_R}{3 \times 10^{16} \text{ G}}\right)^{-1} \times \left(\frac{\rho}{10^{15} \text{ g cm}^{-3}}\right)^{1/2} \left(\frac{R}{15 \text{ km}}\right) \left(\frac{\delta R}{0.1 \text{ km}}\right)^{-1}, \quad (4.6)$$

where we set a spatial scale of the turbulent magnetic field δR as the numerically resolvable scale ≈ 0.1 km, but it should be much smaller than this value in reality.

C. Remark on the angular velocity profile

As shown in Figs. 2 and 3, the radial profile of the angular velocity shows the positive gradient for $R \lesssim 10$ km. However this may not be the case in reality. In our (insufficiently resolved) simulations, the growth timescale of the Kelvin-Helmholtz instability and the timescale of the resultant magnetic-field amplification are longer than the rotational period of the RMNS, which is ~ 1 ms. In reality, however, the growth timescale of the Kelvin-Helmholtz instability should be much shorter than 1 ms. Therefore the Kelvin-Helmholtz vortices and magneto-turbulence could transport the angular momentum within a timescale much shorter than the rotational timescale of the RMNS. This suggests that the angular velocity profile which we found in this paper could be significantly modified. We have to keep in mind this possibility.

V. SUMMARY

We performed high-resolution GRMHD simulations for ≈ 30 ms after merger of a BNS. We carried out a detailed analysis of the MHD-driven turbulence and evaluated the effective viscosity generated by the MRI-driven turbulence (see also Ref. [93] for the Magnetic-Taylor instability as an angular momentum transport agent).

We obtain the convergent result for the α parameter in the RMNS envelope and torus which have low values of density with $\rho < 10^{13}$ g cm $^{-3}$. For the high-density range with 10^{13} g cm $^{-3} \leq \rho \leq 10^{14}$ g cm $^{-3}$, we estimate that the MRI-driven turbulence could generate the effective viscous parameter of ~ 0.01 – 0.02 . For the deep inside the RMNS core with $\rho \geq 10^{14}$ g cm $^{-3}$, the viscous parameter depends significantly on the grid resolution. However, we speculate that the Kelvin-Helmholtz instability and resultant magneto-turbulence could transport the angular momentum in the core region of RMNS. To solve this issue, future ultra high-resolution GRMHD simulations are necessary.

The final goal of this project is to reveal the long-term evolution process of RMNSs formed after BNS mergers. As a next step, we plan to calibrate a viscous hydrodynamical simulation [47, 48] by a GRMHD simulation. Then, we will perform a long-term viscous hydrodynam-

ical simulation to explore the fate of long-lived RMNSs.

ACKNOWLEDGMENTS

We thank C. Ott and M. C. Werner for giving invaluable comments and reading the manuscript carefully. Numerical computation was performed on K computer at AICS (project numbers hp160211 and hp170230), on Cray XC30 at cfca of National Astronomical Observatory of Japan, FX10 and Oakforest-PACS at Information Technology Center of the University of Tokyo, HOKUSAI FX100 at RIKEN, and on Cray XC40 at Yukawa Institute for Theoretical Physics, Kyoto University. This work was supported by Grant-in-Aid for Scientific Research (16H02183, JP16H06342, JP17H01131, 15K05077, 17H06361, 16K17706, 16H06341, 15H00782, 26400237) of JSPS and by a post-K computer project (Priority issue No. 9) of Japanese MEXT.

-
- [1] B. P. Abbott *et al.* [LIGO Scientific and Virgo Collaborations], *Phys. Rev. Lett.* **119**, no. 16, 161101 (2017)
- [2] P. A. Evans *et al.*, *Science* **358**, 1565 (2017)
- [3] M. R. Drout *et al.*, *Science* **358**, 1570 (2017)
- [4] C. D. Kilpatrick *et al.*, *Science* **358**, no. 6370, 1583 (2017)
- [5] M. M. Kasliwal *et al.*, *Science* **358**, 1559 (2017)
- [6] M. Nicholl *et al.*, *Astrophys. J.* **848**, no. 2, L18 (2017)
- [7] Y. Utsumi *et al.* [J-GEM Collaboration], *Publ. Astron. Soc. Japan* **69**, 101 (2017)
- [8] N. Tominaga *et al.*, *Publ. Astron. Soc. Japan* **70**, 28 (2018)
- [9] R. Chornock *et al.*, *Astrophys. J.* **848**, no. 2, L19 (2017)
- [10] I. Arcavi *et al.*, *Astrophys. J.* **848**, no. 2, L33 (2017)
- [11] M. C. Diaz *et al.* [TOROS Collaboration], *Astrophys. J.* **848**, no. 2, L29 (2017)
- [12] B. J. Shappee *et al.*, *Science* **358**, 1574 (2017)
- [13] D. A. Coulter *et al.*, *Science* **358**, 1556 (2017)
- [14] M. Soares-Santos *et al.* [DES and Dark Energy Camera GW-EM Collaborations], *Astrophys. J.* **848**, no. 2, L16 (2017)
- [15] S. Valenti *et al.*, *Astrophys. J.* **848**, no. 2, L24 (2017)
- [16] E. Pian *et al.*, *Nature* **551**, 67 (2017)
- [17] S. J. Smartt *et al.*, *Nature* **551**, no. 7678, 75 (2017)
- [18] D. Haggard, M. Nynka, J. J. Ruan, V. Kalogera, S. Bradley Cenko, P. Evans and J. A. Kennea, *Astrophys. J.* **848**, no. 2, L25 (2017)
- [19] R. Margutti *et al.*, *Astrophys. J.* **848**, no. 2, L20 (2017)
- [20] E. Troja *et al.*, *Nature* **551**, 71 (2017)
- [21] K. D. Alexander *et al.*, *Astrophys. J.* **848**, no. 2, L21 (2017)
- [22] G. Hallinan *et al.*, *Science* **358**, 1579 (2017)
- [23] R. Margutti *et al.*, *Astrophys. J.* **856**, no. 1, L18 (2018)
- [24] D. Dobie *et al.*, arXiv:1803.06853 [astro-ph.HE].
- [25] K. P. Mooley *et al.*, *Nature* **554**, 207 (2018)
- [26] L. -X. Li and B. Paczynski, *Astrophys. J.* **507**, L59 (1998).
- [27] S. R. Kulkarni, astro-ph/0510256.
- [28] B. D. Metzger *et al.*, *Mon. Not. Roy. Astron. Soc.* **406**, 2650 (2010)
- [29] K. Hotokezaka, K. Kiuchi, K. Kyutoku, H. Okawa, Y. i. Sekiguchi, M. Shibata and K. Taniguchi, *Phys. Rev. D* **87**, 024001 (2013)
- [30] T. Dietrich, N. Moldenhauer, N. K. Johnson-McDaniel, S. Bernuzzi, C. M. Markakis, B. Brgmann and W. Tichy, *Phys. Rev. D* **92**, no. 12, 124007 (2015)
- [31] A. Bauswein, S. Goriely and H.-T. Janka, *Astrophys. J.* **773**, 78 (2013)
- [32] S. Bernuzzi, D. Radice, C. D. Ott, L. F. Roberts, P. Moesta and F. Galeazzi, *Phys. Rev. D* **94**, no. 2, 024023 (2016)
- [33] D. Radice, F. Galeazzi, J. Lippuner, L. F. Roberts, C. D. Ott and L. Rezzolla, *Mon. Not. Roy. Astron. Soc.* **460**, no. 3, 3255 (2016)
- [34] C. Palenzuela, L. Lehner, M. Ponce, S. L. Liebling, M. Anderson, D. Neilsen and P. Motl, *Phys. Rev. Lett.* **111**, no. 6, 061105 (2013)
- [35] F. Foucart *et al.*, *Phys. Rev. D* **93**, no. 4, 044019 (2016)
- [36] Y. Sekiguchi, K. Kiuchi, K. Kyutoku and M. Shibata, *Phys. Rev. D* **91**, no. 6, 064059 (2015)
- [37] Y. Sekiguchi, K. Kiuchi, K. Kyutoku, M. Shibata and K. Taniguchi, *Phys. Rev. D* **93**, no. 12, 124046 (2016)
- [38] M. Shibata, S. Fujibayashi, K. Hotokezaka, K. Kiuchi, K. Kyutoku, Y. Sekiguchi and M. Tanaka, *Phys. Rev. D* **96**, no. 12, 123012 (2017)
- [39] S. Fujibayashi, Y. Sekiguchi, K. Kiuchi and M. Shibata, *Astrophys. J.* **846**, no. 2, 114 (2017)
- [40] S. Fujibayashi, K. Kiuchi, N. Nishimura, Y. Sekiguchi and M. Shibata, arXiv:1711.02093 [astro-ph.HE].
- [41] O. Just, M. Obergaulinger, H.-T. Janka, A. Bauswein and N. Schwarz, *Astrophys. J.* **816**, no. 2, L30 (2016)
- [42] D. M. Siegel and B. D. Metzger, *Phys. Rev. Lett.* **119**, no. 23, 231102 (2017)
- [43] R. Fernandez and B. D. Metzger, *Mon. Not. Roy. Astron. Soc.* **435**, 502 (2013)
- [44] R. Fernandez, D. Kasen, B. D. Metzger and E. Quataert, *Mon. Not. Roy. Astron. Soc.* **446**, 750 (2015)
- [45] M. Shibata, Y. Suwa, K. Kiuchi and K. Ioka, *Astrophys. J.* **734**, L36 (2011)

- [46] L. Dessart, C. Ott, A. Burrows, S. Rosswog and E. Livne, *Astrophys. J.* **690**, 1681 (2009)
- [47] M. Shibata, K. Kiuchi and Y. i. Sekiguchi, *Phys. Rev. D* **95**, no. 8, 083005 (2017)
- [48] D. Radice, *Astrophys. J.* **838**, no. 1, L2 (2017)
- [49] K. Kiuchi, K. Kyutoku and M. Shibata, *Phys. Rev. D* **86**, 064008 (2012).
- [50] A. Perego, S. Rosswog, R. M. Cabezn, O. Korobkin, R. Kppeli, A. Arcones and M. Liebendrfer, *Mon. Not. Roy. Astron. Soc.* **443**, no. 4, 3134 (2014)
- [51] S. A. Balbus and J. F. Hawley, *Rev. Mod. Phys.* **70**, 1 (1998).
- [52] S. A. Balbus and J. F. Hawley, *Astrophys. J.* **376**, 214 (1991).
- [53] S. A. Balbus and J. C. B. Papaloizou, *Astrophys. J.* **521**, 650 (1999)
- [54] F. A. Rasio and S. L. Shapiro, *Class. Quant. Grav.* **16** R1-R29 (1999).
- [55] K. Kiuchi, K. Kyutoku, Y. Sekiguchi, M. Shibata and T. Wada, *Phys. Rev. D* **90**, 041502 (2014)
- [56] K. Kiuchi, P. Cerdá-Durán, K. Kyutoku, Y. Sekiguchi and M. Shibata, *Phys. Rev. D* **92**, no. 12, 124034 (2015)
- [57] D. Price and S. Rosswog, *Science*, **312**, 719 (2008).
- [58] Y. T. Liu, S. L. Shapiro, Z. B. Etienne and K. Taniguchi, *Phys. Rev. D* **78**, 024012 (2008)
- [59] D. Neilsen, S. L. Liebling, M. Anderson, L. Lehner, E. O'Connor and C. Palenzuela, *Phys. Rev. D* **89**, no. 10, 104029 (2014)
- [60] M. Anderson, E. W. Hirschmann, L. Lehner, S. L. Liebling, P. M. Motl, D. Neilsen, C. Palenzuela and J. E. Tohline, *Phys. Rev. Lett.* **100**, 191101 (2008)
- [61] M. D. Duez, Y. T. Liu, S. L. Shapiro, M. Shibata and B. C. Stephens, *Phys. Rev. Lett.* **96**, 031101 (2006)
- [62] M. Shibata, M. D. Duez, Y. T. Liu, S. L. Shapiro and B. C. Stephens, *Phys. Rev. Lett.* **96**, 031102 (2006)
- [63] D. M. Siegel, R. Ciolfi, A. I. Harte and L. Rezzolla, *Phys. Rev. D* **87**, no. 12, 121302 (2013)
- [64] M. Obergaulinger, M. A. Aloy and E. Muller, *Astron. Astrophys.* **515**, A30 (2010)
- [65] D. R. Lorimer, *Living Rev. Rel.* **11**, 8 (2008).
- [66] B. Margalit and B. D. Metzger, *Astrophys. J.* **850**, no. 2, L19 (2017)
- [67] B. D. Metzger, T. A. Thompson and E. Quataert, *Astrophys. J.* **856**, no. 2, 101 (2018)
- [68] K. Stovall *et al.*, *Astrophys. J.* **854**, no. 2, L22 (2018)
- [69] P. Lazarus *et al.*, *Astrophys. J.* **831**, no. 2, 150 (2016)
- [70] K. Hotokezaka, K. Kiuchi, K. Kyutoku, T. Muranushi, Y. i. Sekiguchi, M. Shibata and K. Taniguchi, *Phys. Rev. D* **88**, 044026 (2013)
- [71] M. Shibata and T. Nakamura, *Phys. Rev. D* **52**, 5428, (1995).
- [72] T. W. Baumgarte and S. L. Shapiro, *Phys. Rev. D* **59**, 024007 (1998).
- [73] M. Campanelli, C. O. Lousto, P. Marronetti, and Y. Zlochower, *Phys. Rev. Lett.* **96**, 111101 (2006).
- [74] J. G. Baker, J. Centrella, D.-I. Choi, M. Koppitz, and J. van Meter, *Phys. Rev. Lett.* **96**, 111102 (2006).
- [75] A. Kurganov and E. Tadmor, *J. Comput. Phys.* **160**, 241 (2000).
- [76] D. Balsara. *J.Comput.Phys.*,**174**, 614 (2001).
- [77] N. K. Glendenning and S. A. Moszkowski, *Phys. Rev. Lett.* **67**, 2414 (1991).
- [78] J. S. Read, B. D. Lackey, B. J. Owen, and J. L. Friedman, *Phys. Rev. D* **79**, 124032 (2009).
- [79] Note that the magnetic-field strength of the observed BNSs is in the range of $10^{9.7-12.2}$ G [65]. Ultimately, we should explore the consequences due to the small scale magnetic field generated by the Kelvin-Helmholtz instability for the merger dynamics in BNSs with weak initial magnetic field.
- [80] G. Cook, S. L. Shapiro, and S. A. Teukolsky, *Astrophys. J.* **424**, 823 (1994)
- [81] J. D. Kaplan, C. D. Ott, E. P. O'Connor, K. Kiuchi, L. Roberts and M. Duez, *Astrophys. J.* **790**, no. 1, 19 (2014)
- [82] Y. Sekiguchi, K. Kiuchi, K. Kyutoku and M. Shibata, *Phys. Rev. Lett.* **107**, 051102 (2011)
- [83] We construct equilibrium configurations of uniformly rotating relativistic stars with the H4 EOS using a code developed in Ref. [85].
- [84] M. Shibata, K. Taniguchi and K. Uryu, *Phys. Rev. D* **71**, 084021 (2005)
- [85] K. Kiuchi and S. Yoshida, *Phys. Rev. D* **78**, 044045 (2008)
- [86] S. L. Shapiro, *Astrophys. J.* **544**, 397 (2000)
- [87] <http://www2.yukawa.kyoto-u.ac.jp/~kenta.kiuchi/GWRC/>
- [88] J. F. Hawley, X. Guan and J. H. Krolik, *Astrophys. J.* **738**, 84 (2011)
- [89] J. F. Hawley, S. A. Richers, X. Guan and J. H. Krolik, *Astrophys. J.* **772**, 102 (2013)
- [90] A. Brandenburg, *Astrophys. J.* **550**, 824 (1999)
- [91] P. Mösta, C. D. Ott, D. Radice, L. F. Roberts, E. Schnetter and R. Haas, *Nature* **528**, 376 (2015)
- [92] The α -parameter for $10^{10} \text{ g cm}^{-3} \leq \rho \leq 10^{11} \text{ g cm}^{-3}$ is smaller than those in the other regions of the envelope. This might be because the pressure scale height of this density region is larger than the spatial scale determined by the foliation in terms of the density, i.e., our analysis implicitly sets the maximum size of the eddy generated by the MHD instabilities which should be comparable to the pressure scale height.
- [93] M. D. Marshall, M. J., Avara, and J. C. McKinney, arXiv:1709.10113

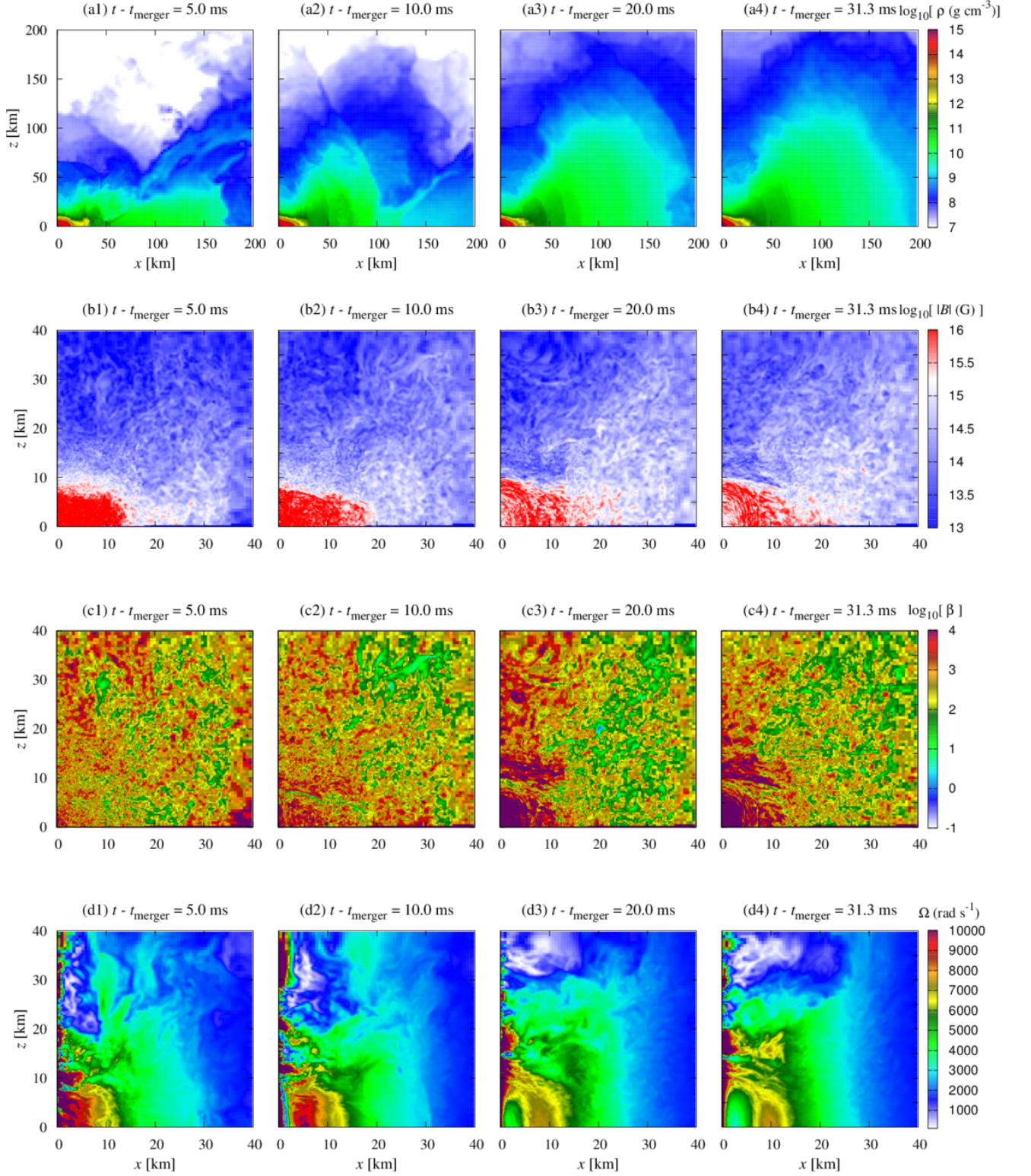


FIG. 1. Profiles of the rest-mass density (panels a1–a4), the magnetic-field strength (panels b1–b4), the plasma beta (panels c1–c4), and the angular velocity (panels d1–d4) on a meridional plane for the 12.5 m run. t_{merger} is the merger time (see text in detail). Note that the panels (a1–a4) show a wider region than the other panels.

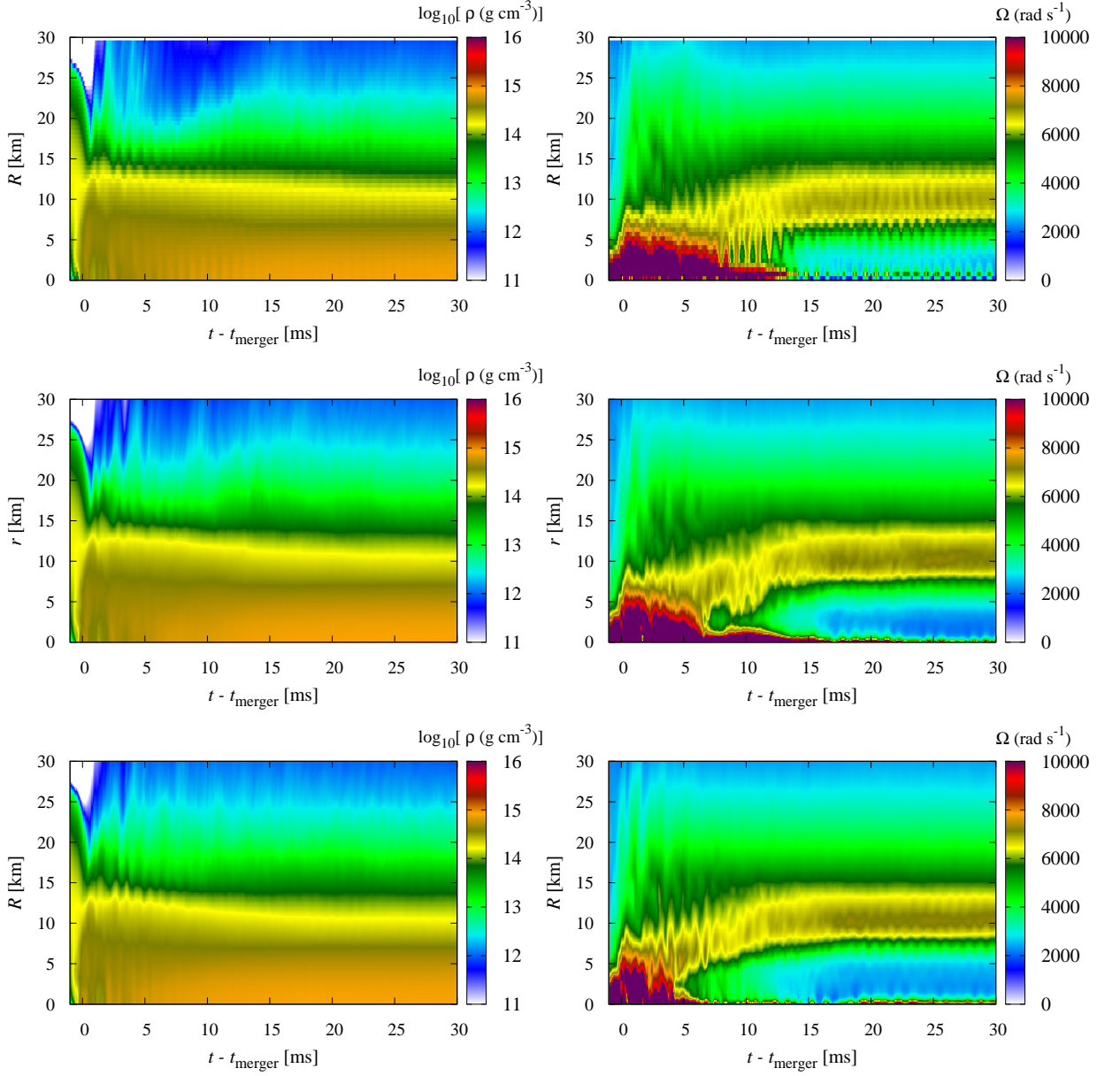


FIG. 2. Spacetime diagrams for the rest-mass density (left) and the angular velocity (right) on the orbital plane for the 12.5 m run (top), the 70 m run (middle), and the 110 m run (bottom). Both profiles are generated by averaging the corresponding quantities along the azimuthal direction.

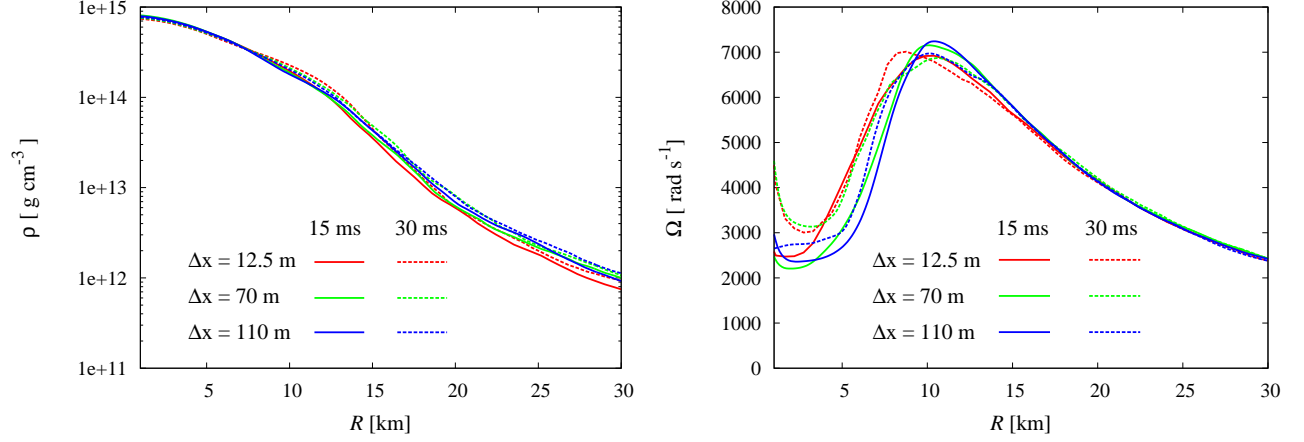


FIG. 3. Radial profiles of the rest-mass density (left) and the angular velocity (right) averaged along the azimuthal direction on the orbital plane at $t - t_{\text{merger}} = 15$ ms and 30 ms.

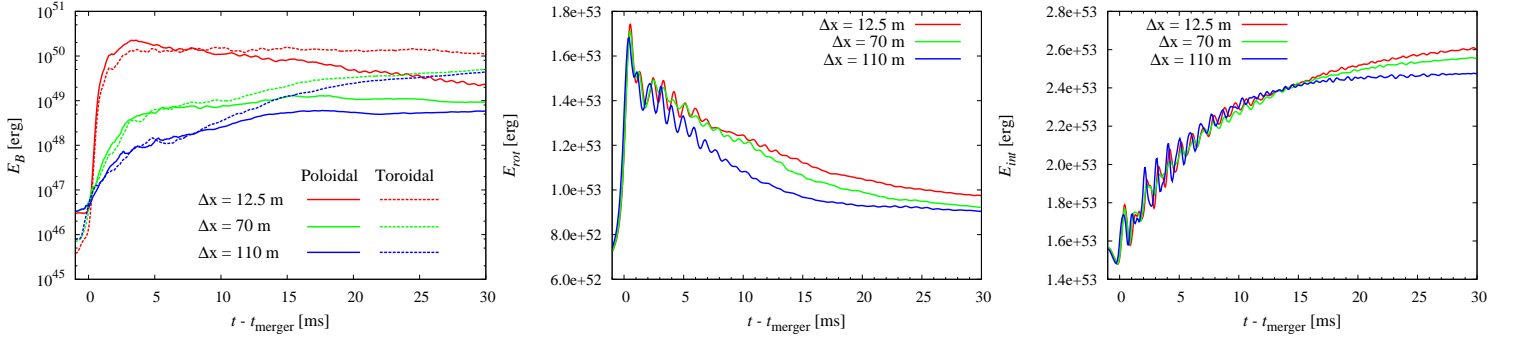


FIG. 4. Magnetic-field energy (left), rotational kinetic energy (center), and internal energy (right) as functions of time for all the runs. The solid and dashed curves in the left panel show the poloidal and toroidal components, respectively.

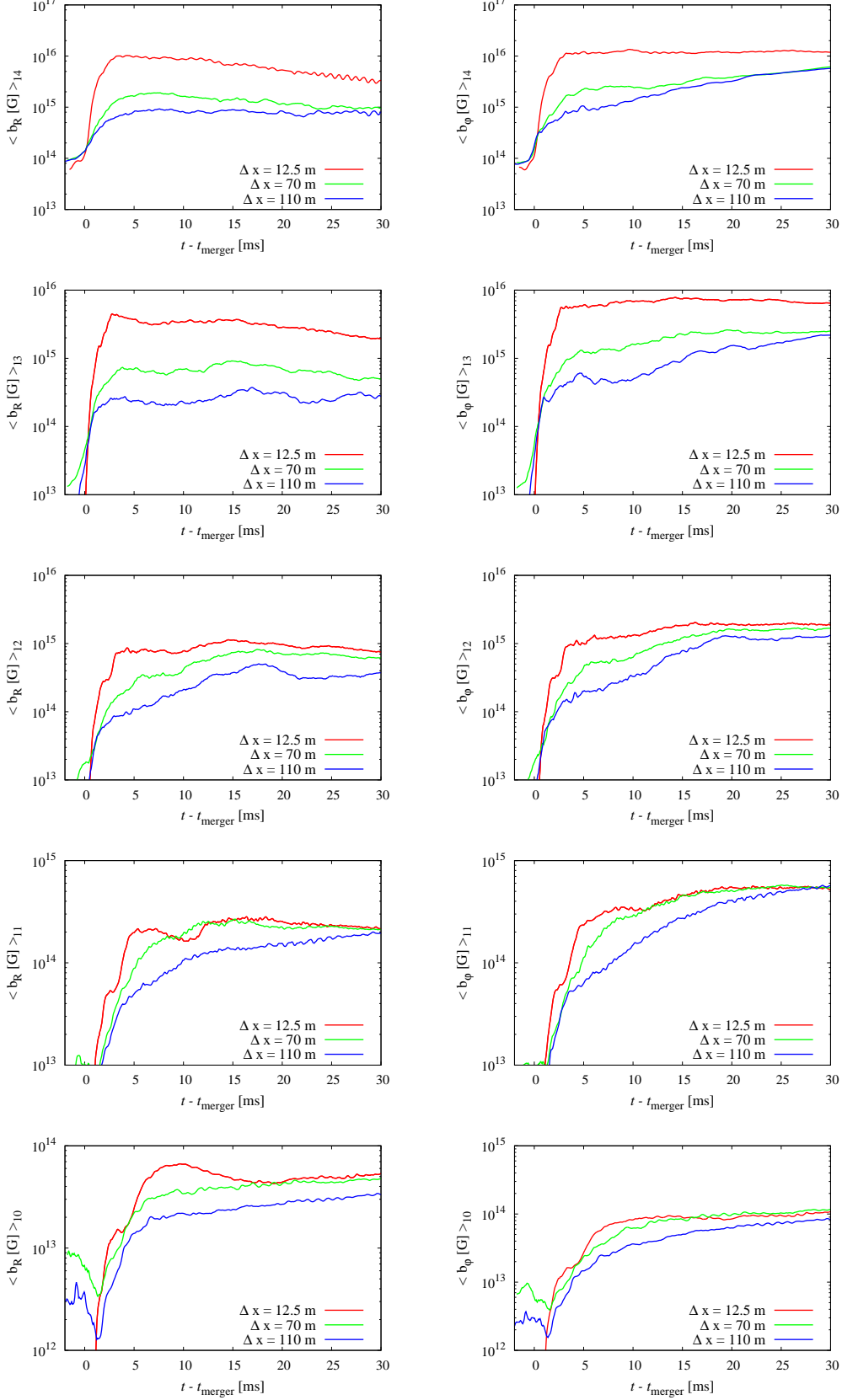


FIG. 5. Volume-averaged radial and azimuthal components of the magnetic field as functions of time. $\langle \cdot \rangle_a$ indicates a volume-average in a density range for $a \leq \log_{10}[\rho \text{ (g cm}^{-3}\text{)}] < a + 1$ with $a = 10\text{--}14$.

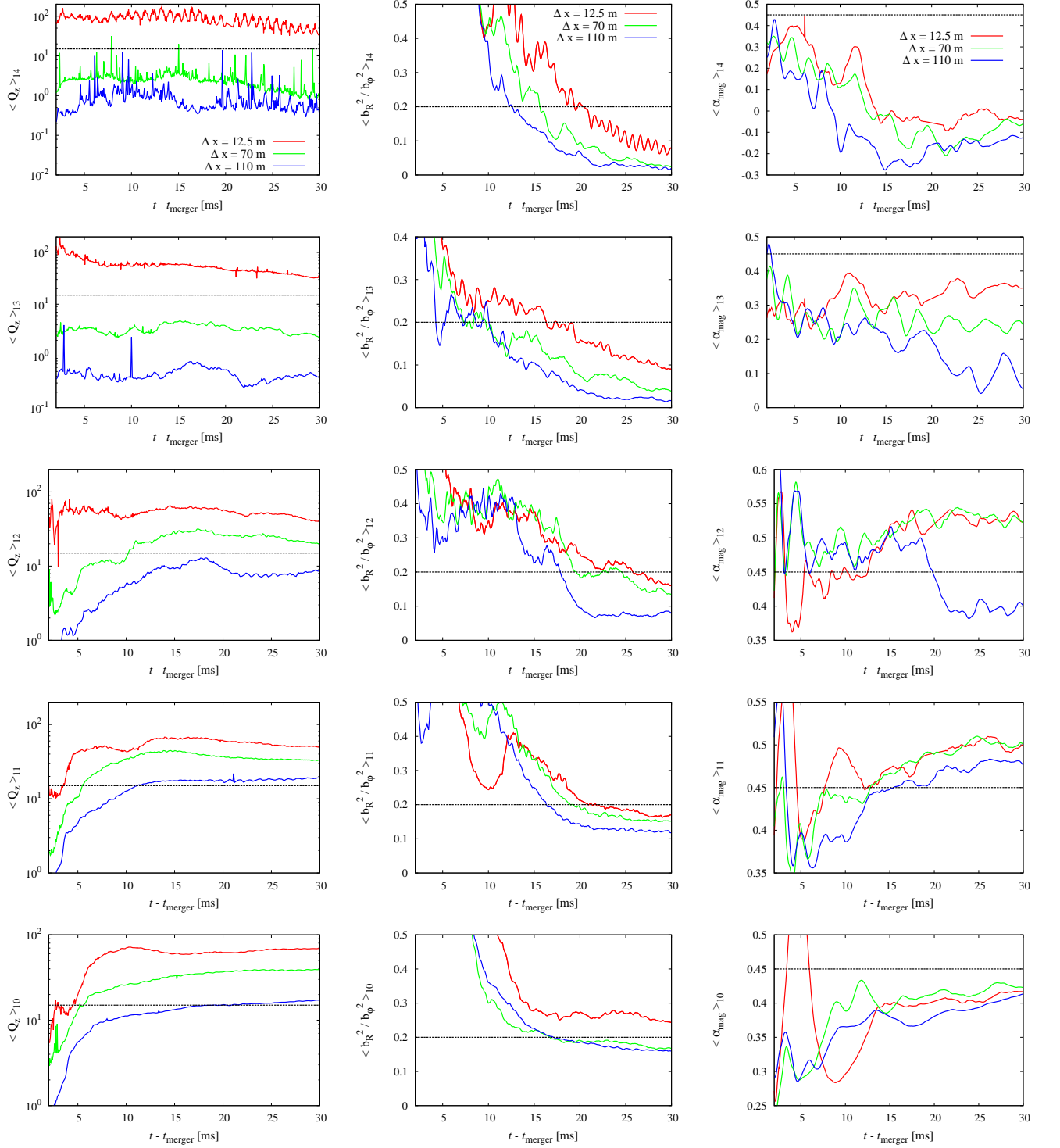


FIG. 6. Volume-averaged convergence metrics Q_z , $\mathcal{R} = b_R^2/b_\phi^2$, and α_{mag} as functions of time. $\langle \cdot \rangle_a$ indicates a volume-average in a density range with $a \leq \log_{10}[\rho \text{ (g cm}^{-3}\text{)}] < a+1$ with $a = 10\text{--}14$. The black-dashed horizontal lines are the criterion above which the MRI-driven turbulence is sustained [88, 89].

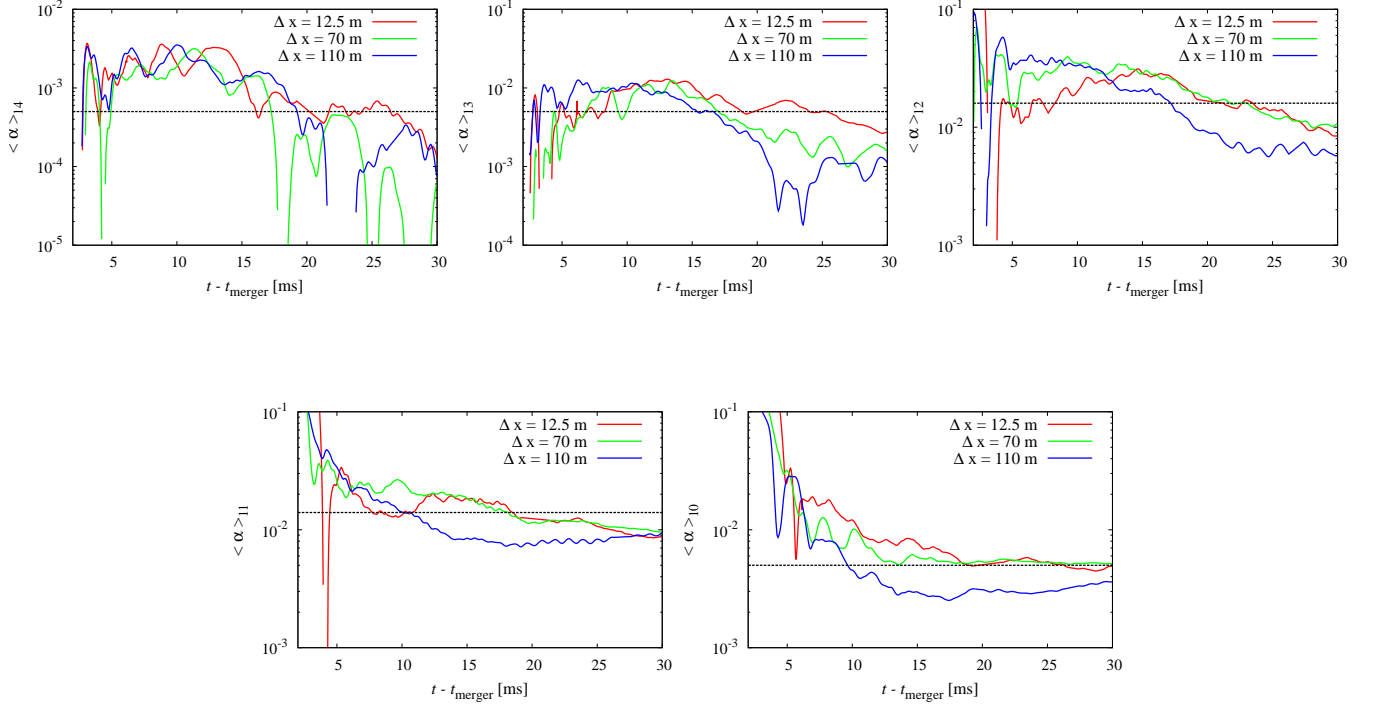


FIG. 7. Same as Fig. 6, but for the α parameter. The black-dashed horizontal lines are the time-averaged values for the 12.5 m run in Table I.

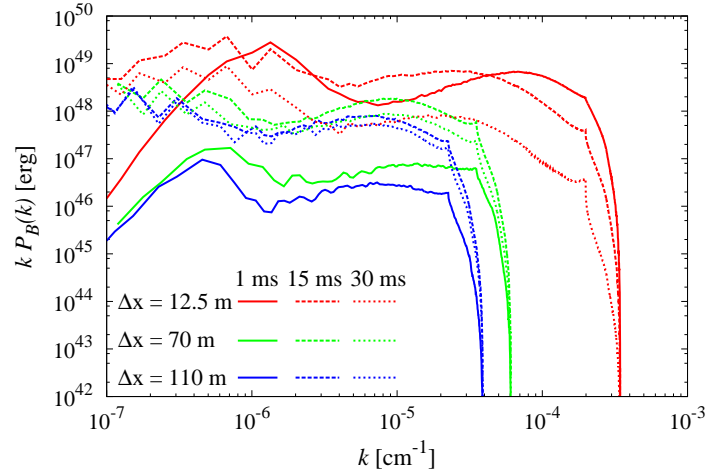


FIG. 8. Spectrum of the poloidal magnetic-field energy for all the runs. Three snapshots with $t - t_{\text{merger}} = 1$ ms, 15 ms, and 30 ms are shown with the solid, dashed, and dotted curves, respectively.

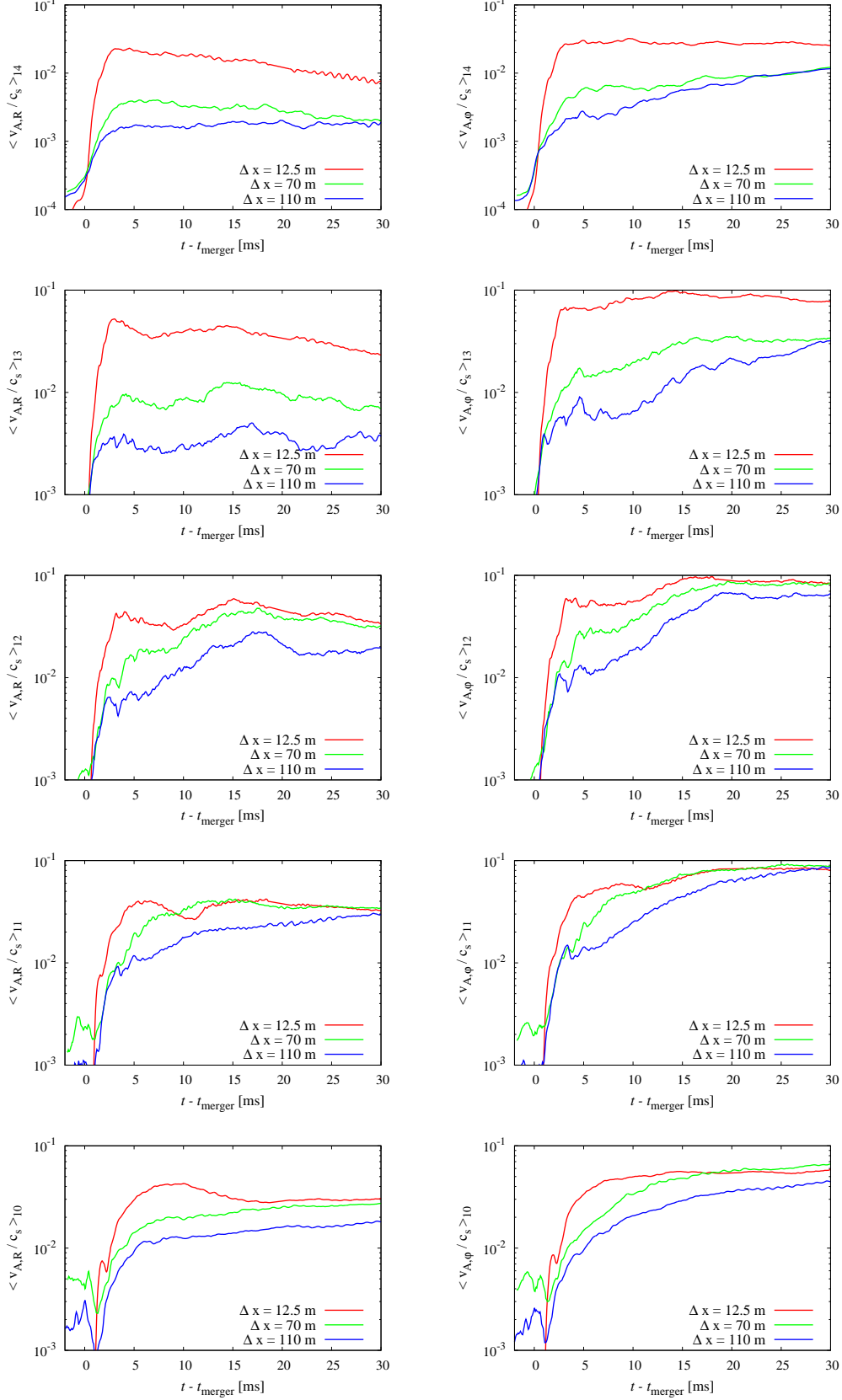


FIG. 9. Volume-averaged Alfvén velocity normalized by the sound speed as functions of time. The left and right columns show the radial and azimuthal component, respectively. $\langle \cdot \rangle_a$ indicates a volume-average in a density range with $a \leq \log_{10}[\rho \text{ (g cm}^{-3}\text{)}] < a + 1$ with $a = 10\text{--}14$.

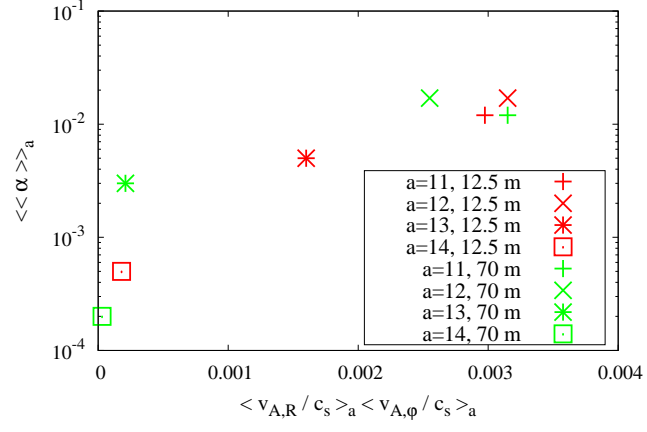


FIG. 10. Time- and volume-averaged α parameter as a function of $\langle v_{A,R}/c_s \rangle_a \langle v_{A,\varphi}/c_s \rangle_a$ for $a = 11-14$. We show the results of the 12.5 m run and the 70 m run.